Special Issue: Revisiting Materials Challenges from the Perspective of Energy Applications

Thermodynamic Modeling of Oxide Phases in the Mn-O System

YOUN-BAE KANG and IN-HO JUNG

A critical evaluation and thermodynamic modeling for thermodynamic properties of all oxide phases and phase diagrams in the Mn-O system are presented. Optimized Gibbs energy parameters for the thermodynamic models of the oxide phases were obtained which reproduce all available and reliable experimental data within error limits from 298 K (25 °C) to above the liquidus temperature at compositions covering from MnO to MnO_2, and oxygen partial pressure from 10^{-15} to 10^{2} (bar). The optimized thermodynamic properties and phase diagrams are believed to be the best estimates presently available. Two spinel phases (α- and β-Mn_3O_4) were modeled using Compound Energy Formalism (CEF) with the use of physically meaningful parameters. Valence states of the spinels are interpreted based on the available thermopower measurement, for which Mn^{4+} was considered in the cubic spinel (β-Mn_3O_4). The present Mn_3O_4 spinel solutions can be integrated into a larger spinel solution database, which has been already developed. The database of the model parameters can be used along with a software for Gibbs energy minimization in order to calculate any type of phase diagram sections and thermodynamic properties.

DOI: 10.1007/s40553-016-0083-z

I. INTRODUCTION

MANGANESE oxides are of great interest in metallurgical fields (iron and steelmaking, ferroalloy production), since the manganese plays an important role as a major alloying element in steel, and manganese silicate is one of the abundant inclusions in steels. Also manganese oxides have been interesting materials for their applications to oxide fuel cell as one of the energy materials, and magnetic storage materials. Mn nodule under pacific ocean also has been interesting as noble metal resources. Therefore, knowledge for the manganese oxide containing system is valuable to the industries. In this regard, a research on the thermodynamic properties and phase equilibria in the Mn-O system is necessary. Extensive reviews of several investigations and comparisons of data obtained in the Mn-O system were given by Wang and Sundman[1] and Grundy *et al.*[2] by critical evaluations and thermodynamic assessments.

Apart from metallic Mn (α-, β-, γ-, δ-Mn and L-Mn), the Mn-O system is composed of the following phases: manganosite ($Mn_{1-x}O$), hausmannite (α- and β-Mn_3O_4), bixbyite (α- and β-Mn_2O_3), pyrolusite (MnO_2), and liquid oxide (slag). Mn may exist as divalent, trivalent, and tetravalent ions in those oxide phases depending on phase, temperature, and oxygen partial pressure. Non-stoichiometries of the Mn_2O_3 and MnO_2 are very small, while manganosite deviates considerably from its stoichiometry at high temperature/oxygen partial pressure. Non-stoichiometries of α- and β-Mn_3O_4 were observed.[3]

The earlier thermodynamic assessment by Wang and Sundman[1] used Compound Energy Formalism[4] to model the manganosite and Two Sublattice Ionic Model[5] for the liquid phase which extends from metallic liquid to ionic liquid. Other phases were regarded as stoichiometric compounds. Later, Grundy *et al.*[2] pointed out that the thermodynamic description of Wang and Sundman[1] had some flaws and they re-assessed the Mn-O system using the same modeling approach but different set of model parameters. In both studies, α- and β-Mn_3O_4 were treated as stoichiometric compounds.

However, when an optimized thermodynamic database of the Mn-O system is to be integrated into an already developed large thermodynamic database, keeping consistency between the databases is indispensible. Since the manganese spinels (α- and β-Mn_3O_4, both) form extensive solid solutions with Fe, Al, Cr, Co, Mg, *etc.*,[6] α-Mn_3O_4 and β-Mn_3O_4 have to be modeled as a part of larger thermodynamic database of spinel solid solution, for example, developed at the CRCT, École Polytechnique de Montréal.[7] Therefore, in the present study, it has been attempted to

YOUN-BAE KANG, Associate Professor, is with the Graduate Institute of Ferrous Technology, Pohang University of Science and Technology, Pohang, 37673, Republic of Korea. Contact e-mail: ybkang@postech.ac.kr IN-HO JUNG, Associate Professor, is with the Department of Mining and Materials Engineering, McGill University Montreal, QC, H3A 2B2, Canada.

Manuscript submitted January 13, 2016.
Article published online June 2, 2016

model both α-Mn_3O_4 and β-Mn_3O_4 spinels as solutions, not stoichiometric compounds. Recently, Kjellqvist and Selleby updated thermodynamic modeling of the Mn-O system by Grundy *et al.*,[2] by taking into account the two spinel phases as a part of larger solution composed of Fe-Mn-O,[8] but only limited results were presented in their article.

The present study is a part of a complete database development of the Al_2O_3-CaO-CoO-CrO-Cr_2O_3-Cu_2O-FeO-Fe_2O_3-MgO-MnO-Mn_2O_3-NiO-PbO-SiO_2-TiO_2-Ti_2O_3-ZnO systems for applications in the ferrous, non-ferrous, ceramic, and electric/electronic industries. In particular, in conjunction with the present study of Mn oxide, critical evaluation and thermodynamic optimization for the Mn-Cr-O system were already published,[9] and those of Fe-Mn-O, Mn-Si-O, and Fe-Mn-Si-O systems will be described elsewhere.[10,11] Some of the results obtained in the present study was presented in a conference proceeding.[12] All the thermodynamic calculations in the present study were carried out using FactSage.[13,14]

II. THERMODYNAMIC MODELS

Figure 1 shows a phase diagram of the Mn-O system as a function of temperature and oxygen partial pressure, calculated from the thermodynamic models of the present study. The following phases are found in this system: Slag, $Mn_{1-x}O$, α-Mn_3O_4, β-Mn_3O_4, α-Mn_2O_3, β-Mn_2O_3, MnO_2, α-Mn, β-Mn, γ-Mn, δ-Mn, and liquid Mn (L-Mn).

A. α-Mn_3O_4 and β-Mn_3O_4 (Spinel)

Thermodynamic models for the spinel solutions were developed using two sublattice model within the framework of the Compound Energy Formalism (CEF).[22] Using the model, a thermodynamic database for a multicomponent spinel composed of Al-Co-Cr-Fe-Mg-Ni-Zn-O has been developed.[7] In the present study, this model was extended to incorporate Mn. Moreover, since the model and the database were previously developed only for the cubic spinel, a new thermodynamic model using the similar approach (CEF) was developed for the tetragonal spinel (α-Mn_3O_4).

In the cubic spinel, oxygen ions form a fcc close packing structure. Cations occupy half of octahedral interstices and one-eighth of tetrahedral interstices. The number of the octahedral sites is twice the number of the tetrahedral sites. Therefore, a formula unit of spinel may be written as $(i)^{\mathrm{T}}[j]_2^{\mathrm{O}}\mathrm{O}_4$. For the tetragonal spinel, the same close packing scheme of oxygen in the tetragonal structure may be used. Additional interstitial site to describe a deviation toward Mn side was not considered in the present study.

The Gibbs energy expression in the CEF per formula unit of spinel is

$$G = \sum_i \sum_j y_i^{\mathrm{T}} y_j^{\mathrm{O}} G_{ij} - TS^{\mathrm{config}} + G^{\mathrm{excess}} + G^{\mathrm{magnetic}}, \quad [1]$$

where y_i^{T} and y_j^{O} represent the site fractions of species i and j on the tetrahedral and octahedral sites, and G_{ij} is the Gibbs energy of an "end-member" $(i)^{\mathrm{T}}[j]_2^{\mathrm{O}}\mathrm{O}_4$ of the solution, in which the first sublattice is occupied only by the species i and the second sublattice only by the species j. S^{config} is the configurational entropy assuming random mixing on each sublattice:

$$S^{\mathrm{config}} = -\mathrm{R}\left(\sum_i y_i^{\mathrm{T}} \ln y_i^{\mathrm{T}} + 2\sum_j y_j^{\mathrm{O}} \ln y_j^{\mathrm{O}}\right). \quad [2]$$

G^{magnetic} is the contribution of magnetic properties on the Gibbs energy, which is explained in Section II–E.

Since the Mn_3O_4 exhibits two different structures (tetragonal and cubic), thermodynamic modeling was carried out separately in the present study.

1. α-Mn_3O_4 (tetragonal spinel)

For the tetragonal Mn_3O_4 spinel solution, the following model structure was considered:

$$\left(\mathrm{Mn}^{2+}, \mathrm{Mn}^{3+}\right)^{\mathrm{T}}\left[\mathrm{Mn}^{2+}, \mathrm{Mn}^{3+}, \mathrm{Va}\right]_2^{\mathrm{O}}\mathrm{O}_4, \quad [3]$$

for which the reason is discussed in detail in Section III–B.

In the present study, no excess Gibbs energy terms were required, that is $G^{\mathrm{excess}} = 0$. The Gibbs energy of the tetragonal spinel solution is thus fully defined by the Gibbs energies G_{ij} of the six end-members. These are denoted as G_{JJ}, G_{JK}, G_{JV}, G_{KJ}, G_{KK}, and G_{KV}, where J, K, and V mean Mn^{2+}, Mn^{3+}, and Va, respectively. These are also connected each other by certain linear combinations of the G_{ij}, having physical sense as

$$G_{\mathrm{JK}}, \quad [4]$$

$$G_{\mathrm{KJ}} = G_{\mathrm{JK}}, \quad [5]$$

$$G_{\mathrm{KK}} = G_{\mathrm{JK}} + I_{\mathrm{JK}}, \quad [6]$$

$$G_{\mathrm{JJ}} = G_{\mathrm{JK}} - I_{\mathrm{JK}} + \Delta_{\mathrm{JK}}, \quad [7]$$

$$G_{\mathrm{KV}} = 8G^{\circ}(\mathrm{Mn_2O_3}, \gamma) - 2\mathrm{R}T(5\ln 5 - 6\ln 6) - 5G_{\mathrm{JK}} - 5I_{\mathrm{JK}}, \quad [8]$$

$$G_{\mathrm{JV}} = \Delta_{\mathrm{JK}} - \Delta_{\mathrm{KJV}} - 6I_{\mathrm{JK}} + 8G^{\circ}(\mathrm{Mn_2O_3}, \gamma) - 2\mathrm{R}T(5\ln 5 - 6\ln 6) - 5G_{\mathrm{JK}}. \quad [9]$$

G_{JK} represents a Gibbs energy of $(\mathrm{Mn}^{2+})^{\mathrm{T}}[\mathrm{Mn}^{3+}]_2^{\mathrm{O}}\mathrm{O}_4$ end-member in the tetragonal spinel structure. G_{KJ} was set to the same to G_{JK} as the reference state for charged end-members of spinels, as was done for cubic spinel.[22] I_{JK} was used to set G_{KK}, and represents degree of inversion of cation distribution. Δ_{JK} was used to set G_{JJ}. Gibbs energy of end-members containing Va (G_{KV} and G_{JV}) were described by Eqs. [8] and [9], using Gibbs energy of a hypothetical "γ-Mn_2O_3" (Mn deficient spinel structure). The Gibbs energy of the "γ-Mn_2O_3" was optimized in order to model experimentally observed

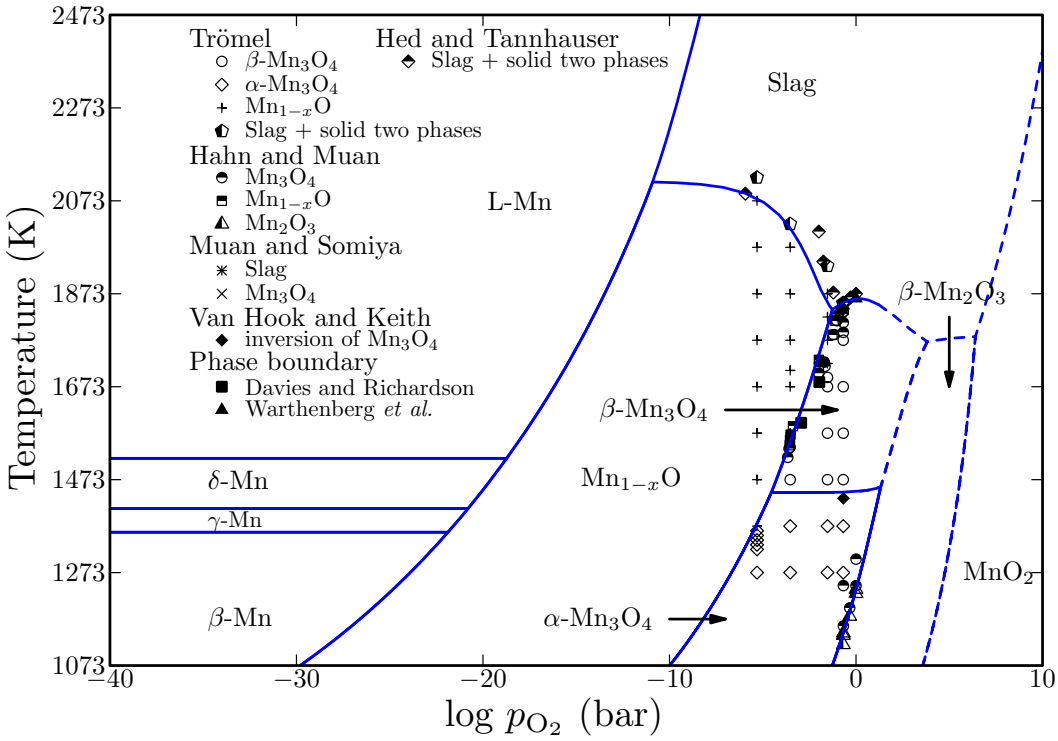

Fig. 1—Calculated phase diagram of the Mn-O system along with experimental data.[20,21,55,67–70]

Table I. Optimized Model Parameters for Tetragonal Spinel Phases

Tetragonal Spinel: $(Mn^{2+}, Mn^{3+})^{T}[Mn^{2+}, Mn^{3+}, Va]_2^{O}O_4$*
$G_{JK} = 7 \times (-200290.47 - 2.56T - 0.002914T^2 - 0.0001736T^3)$, $T < 70\,K$
$= 7 \times (-192269.76 + 209.89T - 32.27T\ln T - 41304.25T^{-1} - 364.67T^{-0.5} - 2290.5\ln T)$, $70\,K < T < 1445\,K$
$G_{KJ} = G_{JK}$
$G_{KK} = G_{JK} + I_{JK}$
$G_{JJ} = G_{JK} - I_{JK} + \Delta_{JK}$
$G_{KV} = 8G^{\circ}(Mn_2O_3,\gamma) - 2RT(5\ln 5 - 6\ln 6) - 5G_{JK} - 5I_{JK}$, where $G^{\circ}(Mn_2O_3,\gamma) = G^{\circ}(Mn_2O_3,\beta) + 20{,}920$
$G_{JV} = \Delta_{JK} - \Delta_{KJV} - 6I_{JK} + 8G^{\circ}(Mn_2O_3,\gamma) - 2RT(5\ln 5 - 6\ln 6) - 5G_{JK}$
$I_{JK} = G_{KK} + G_{KJ} - 2G_{JK} = 98{,}324$
$\Delta_{JK} = G_{JJ} + G_{KK} - G_{JK} - G_{KJ} = 40{,}000$
$\Delta_{KJV} = G_{JJ} + G_{KV} - G_{KJ} - G_{JV} = -941190.8 + 627.6T$
Magnetic properties
$\beta_{JK} = \beta^{i}_{JK} = -3 \times 7.91$ (average magnetic moment per atom)
$T_{JK} = T^{i}_{JK} = -3 \times 43.19\,K$ (Néel temperature)
$p = 0.28$

*Notation A, E, J, K, L and V are used for Fe^{2+}, Fe^{3+}, Mn^{2+}, Mn^{3+}, Mn^{4+} and vacancy, respectively.

non-stoichiometry of α-Mn_3O_4[3] toward O-rich side, assuming an ideal dissolution of a hypothetical "γ-Mn_2O_3" (Mn deficient spinel structure) in the spinel.

All the parameters are listed in Table I.

2. *Cubic spinel solution (β-Mn_3O_4)*

For the cubic Mn_3O_4 spinel solution, the following model structure was considered:

$$(Mn^{2+})^{T}[Mn^{2+}, Mn^{3+}, Mn^{4+}, Va]_2^{O}O_4\,, \qquad [10]$$

for which the reason is discussed in detail in Section III–B. As was done for the tetragonal spinel, no excess Gibbs energy terms were required, that is $G^{excess} = 0$. The Gibbs energy of the cubic spinel solution is thus fully defined by the Gibbs energies G_{ij} of the four end-members. These are denoted as G_{JJ}, G_{JK}, G_{JL}, and G_{JV}, where J, K, L, and V mean Mn^{2+}, Mn^{3+}, Mn^{4+}, and Va, respectively. Since the present study is part of a larger effort aimed at developing a complete database for multicomponent spinel, it is

necessary to maintain consistency in parameters which are common to several sub-systems. Therefore, although only Mn_3O_4 spinel is considered in this article, the Gibbs energies of end-members G_{ij} in the Mn-O system are linked to the Gibbs energies of end-members in other sub-systems. In the present study, Gibbs energies of end-members in the Fe_3O_4,[22] and $(Fe,Mn)_3O_4$[10] which was simultaneously optimized in the present study, were used as parts of Gibbs energies of end-members in the β-Mn_3O_4. Also, certain linear combinations of the G_{ij}, which have physical sense, are used as the optimized model parameters. These linear combinations are related each other as

$$G_{JK}\,, \qquad [11]$$

$$G_{JJ} = -2G_{AE} - 2I_{AE} + 3G_{JE} + I_{JE} + \Delta_{JE}\,, \qquad [12]$$

$$G_{JL} = 2G_{JK} - G_{JJ} + \Delta_{JL}\,, \qquad [13]$$

$$G_{JV} = \frac{5}{7}G_{JK} + V_x\,, \qquad [14]$$

where A and E represent Fe^{2+} and Fe^{3+}, respectively. G_{JK} represents Gibbs energy of $(Mn^{2+})^{T}[Mn^{3+}]_2^{O}O_4$ end-member in the cubic spinel structure. V_x is used to set G_{JV} in order to reproduce non-stoichiometry of β-Mn_3O_4 toward O-rich side, followed by the suggestion of Degterov *et al.*[22] Δ_{JL} is used to set G_{JL} in order to reproduce the degree of inversion. Description of G_{JJ} is connected to the Gibbs energy of other end-members in the Fe–O system[22] and those in the Fe–Mn-O system, which can be found elsewhere.[10] All the parameters are listed in Table II.

B. *Slag (Molten Oxide)*

For the slag (molten oxide) phase, the Modified Quasichemical Model in the pair approximation (MQM) was used.[15,16] This model has been recently further developed and summarized.[17,18] Short-range ordering (SRO) is taken into account by considering second-nearest neighbor (SNN) pair exchange reactions. For example, for the MnO-$MnO_{1.5}$ slag, this reaction is

$$\begin{aligned}(Mn^{2+} - O - Mn^{2+}) + (Mn^{3+} - O - Mn^{3+}) \\ = 2(Mn^{2+} - O - Mn^{3+}) \quad \Delta g_{Mn^{2+}Mn^{3+}}\end{aligned}\,, \qquad [15]$$

where (*i*-O-*j*) represents a SNN pair. The parameter of the model is the Gibbs energy of this pair forming reaction, $\Delta g_{Mn^{2+}Mn^{3+}}$, which may be expanded as empirical functions of composition. There being no evidence to the contrary in the present optimization, it was assumed that only Mn^{2+} and Mn^{3+} are considered for the molten oxide. "Coordination numbers" of Mn^{2+} and Mn^{3+} required in the MQM were set to be 1.3774 ($Z_{Mn^{2+}Mn^{2+}}$) and 2.0662 ($Z_{Mn^{3+}Mn^{3+}}$), respectively. Gibbs energy of pure liquid MnO was taken from Wu *et al.*[19] However, a pure liquid "Mn_2O_3" is not stable under normal condition, and its thermodynamic properties has not been known. Therefore, in the present study, the Gibbs energy of hypothetical liquid "Mn_2O_3" was assumed to be 2.5 times of Gibbs energy of the pure liquid MnO, and an additional enthalpic term was used as a model parameter during optimization in order to reproduce measured liquidus temperatures[20,21] (Actual model component is $MnO_{1.5}$, not Mn_2O_3). $\Delta g_{Mn^{2+}-Mn^{3+}}$ was set to zero. The optimized thermodynamic values for the molten oxide are shown in Table III.

C. *Manganosite Solution ($Mn_{1-x}O$)*

The manganosite solution of rock-salt structure was modeled as a simple random mixture of Mn^{2+} and Mn^{3+} ions on cation site using a simple polynomial excess Gibbs energy. It is assumed that cation vacancies associate with the Mn^{3+} cation in order to maintain electrical neutrality and do not contribute to the configurational entropy independently. The Gibbs energy per mole of the solution is given as

$$\begin{aligned}G = &X_{Mn^{2+}}G_{MnO} + X_{Mn^{3+}}G_{MnO_{1.5}} \\ &+ RT(X_{Mn^{2+}}\ln X_{Mn^{2+}} + X_{Mn^{3+}}\ln X_{Mn^{3+}}) \\ &+ X_{Mn^{2+}}X_{Mn^{3+}}L_{Mn^{2+}Mn^{3+}}\end{aligned} \qquad [16]$$

Table II. Optimized Model Parameters for Cubic Spinel Phases

Cubic Spinel: $(Mn^{2+})^{T}[Mn^{2+}, Mn^{3+}, Mn^{4+}, Va]_2^{O}O_4$*
$G_{JK} = 7 \times (-189699.33 + 207.82T - 32.27T\ln T - 41304.25T^{-1} - 364.67T^{-0.5} - 2290.5\ln T)$
$G_{JJ} = -2G_{AE} - 2I_{AE} + 3G_{JE} + I_{JE} + \Delta_{JE}$
$G_{JL} = 2G_{JK} - G_{JJ} + \Delta_{JL}$
$G_{JV} = \frac{5}{7}G_{JK} + V_x$
$\Delta_{JL} = 26210 - 17.46T$
$V_x = 679021.36 - 264.99T$
$G_{AE} = 7 \times (-161655.14 + 144.93T - 0.00116417T^2 - 24.976T\ln T + 206468T^{-1})$[22]
$I_{AE} = -31229 + 22.063T$
$G_{JE} = 7 \times (-183138 + 167.46T - 28.11T\ln T + 227857T^{-1})$[10]
$I_{JE} = 16963.13 + 16.79T$[10]
$\Delta_{JE} = 40{,}000$[10]

*Notation A, E, J, K, L and V are used for Fe^{2+}, Fe^{3+}, Mn^{2+}, Mn^{3+}, Mn^{4+} and vacancy, respectively. G_{AE} and I_{AE} are a Gibbs energy of end-member and a model parameter used in the Fe_2O_4 spinel and are given in Degterov *et al.*[22] G_{JE}, I_{JE} and Δ_{JE} are a Gibbs energy of end-member and model parameters used in the $(Fe,Mn)_3O_4$ spinel and are given in Kang and Jung.[10]

Table III. Optimized Model Parameters for Slag, Manganosite, and Stoichiometric Compounds

Manganosite: (MnO-$MnO_{1.5}$)

$G(MnO) = G^{\circ}(MnO, \text{solid})$*

$G(MnO_{1.5}) = 0.5G^{\circ}(Mn_2O_3, \beta) + 12001.8 - 4.87T$

$q^{20}_{MnO,MnO_{1.5}} = 20{,}920$

Slag: (MnO-$MnO_{1.5}$)**

$G(MnO) = G^{\circ}(MnO, \text{liquid})$*

$G(MnO_{1.5}) = 1.25G^{\circ}(MnO, \text{liquid}) + 25731.6$

$\Delta g_{Mn^{2+}Mn^{3+}} = 0$

Stoichiometric compounds

$$G(Mn_2O_3, \alpha) = -961204.54 - 10.27T - 0.075T\ln T - 40.833 \times 10^{-5}T^3,\ T < 100\,\text{K}$$
$$= -963053.57 + 672.49T - 96.35T\ln T - 0.0927T^2 - 3028.61T^{0.5},\ 100\,\text{K} < T < 308\,\text{K}\ \text{(Néel temperature)}$$
$$\beta = -3 \times 2.439,\ T_N = -3 \times 79.45$$

$$G(Mn_2O_3, \beta) = -1512892.14 + 26796.59T - 5081T\ln T + 15.56T^2 - 0.0081T^3,\ 308\,\text{K} < T < 320\,\text{K}$$
$$-945439.49 + 813.45T - 133.5T\ln T - 0.006T^2 + 143152.38T^{-1} - 10000\ln T,\ 320\,\text{K} < T$$

$$G(MnO_2) = -526358.49 - 7.80T - 0.015T\ln T - 9.83 \times 10^{-7}T^4,\ T < 113\,\text{K}$$
$$= -521554.48 + 947.57T - 126.28T\ln T - 5738.46T^{0.5} + 3246.06\ln T,\ 113\,\text{K} < T\ \text{(Néel temperature)}$$
$$\beta = -3 \times 1.5562,\ TN = -3 \times 92.2$$

* Parameters of the MQM is defined in Ref. [17].

** The Gibbs energies of pure solid and liquid MnO were taken from Wu *et al.*[19]

where $L_{Mn^{2+}Mn^{3+}}$ may be expanded as a function of polynomial:

$$L_{Mn^{2+}Mn^{3+}} = \sum_{i,j\geq 0} q^{ij}_{Mn^{2+}Mn^{3+}} X^i_{Mn^{2+}} X^j_{Mn^{3+}} \qquad [17]$$

D. *Metallic Phases*

All metallic Mn (α-Mn, β-Mn, γ-Mn, δ-Mn, and L-Mn) were treated as stoichiometric phases and their Gibbs energies were taken from Dinsdale.[23]

E. *Magnetic Properties*

α-Mn_3O_4, α-Mn_2O_3, and MnO_2 have magnetic transition associated with Néel temperatures. Their magnetic contributions to the Gibbs energies were considered by an empirical relationship suggested by Inden[24] and modified by Hillert and Jarl.[25] Although the suggested Gibbs energy equation for the magnetic property was developed for cubic (FCC, BCC) and hexagonal (HCP) structures,[25] in the present study, the same equation with the same p factor for FCC (p = 0.28) was assumed for α-Mn_3O_4 (tetragonal), α-Mn_2O_3 (orthorhombic), and MnO_2 (tetragonal) phases.

III. CRITICAL EVALUATION OF EXPERIMENTAL DATA AND THERMODYNAMIC OPTIMIZATION

A. *Thermodynamic and Magnetic Properties*

Gibbs energy of stoichiometric MnO was taken from Wu *et al.*[19]

Low-temperature heat capacities and heat contents of Mn_3O_4, Mn_2O_3, and MnO_2 were measured by a number of researchers. Millar measured the heat capacities of Mn_3O_4 and MnO_2 calorimetrically down to ~72 K (−201 °C).[26] He did not observe λ-type anomaly of hear capacity of Mn_3O_4, which was later found by Robie and Hemingway[27] and Chhor *et al.*[28] at ~43 K (−230 °C). Also, the measured heat capacity of MnO_2 by Millar is systematically higher than later measurements by Robie and Hemingway[27] and Kelley and Moore.[29] Kelley and Moore pointed out that Millar's calibration on his calorimeter had small error which caused the systematic error. Other measurements of the heat capacities of Mn_2O_3 by King[30] and Robie and Hemingway[27] were in good agreement with each other. Robie and Hemingway also observed a broad change of heat capacity near 307.5 K (34.5 °C), which is associated with the orthorhombic to cubic transition discovered by Geller and Espinosa.[31] All the measured heat capacity data are shown in Figures 2 through 4 with optimized heat capacities in the present study. By fitting the heat capacities considering magnetic transitions, the third law entropies for these phases were calculated as 168.06 J/mol·K for the Mn_3O_4, 115.78 J/mol K for the Mn_2O_3, and 53.48 J/mol K for the MnO_2, while the reported values are in the ranges of 154.07 to 167.1 J/mol K for the Mn_3O_4, 110.5 to 113.7 J/mol K for the Mn_2O_3, and 52.75 to 58.32 J/mol K for the MnO_2.[2] All these phases experience phase transitions from the antiferromagnetic to the paramagnetic states and corresponding Néel temperatures are shown in Tables I and III along with optimized magnetic momentum β. Large heat capacity data of α-Mn_3O_4 at the magnetic transition temperature observed by Robie and Hemingway[27] and Chhor *et al.*[28] could not be accounted for by the current magnetic model of Hillert and Jarl.[25]

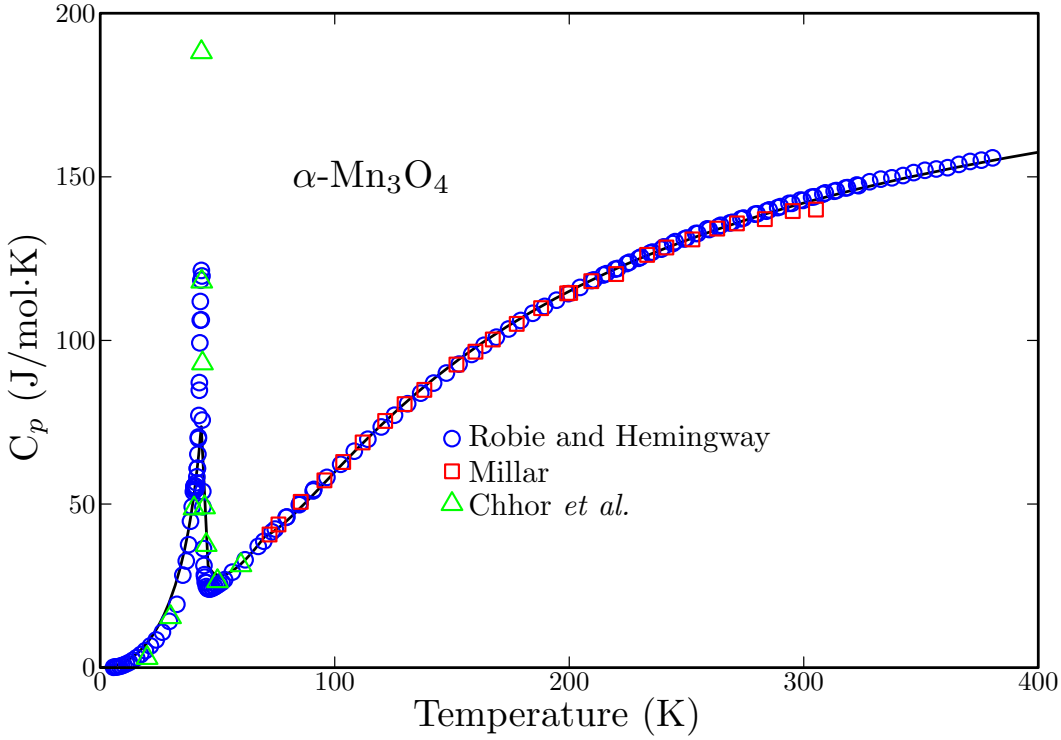

Fig. 2—Optimized heat capacity of α-Mn_3O_4 along with experimental data.[26–28]

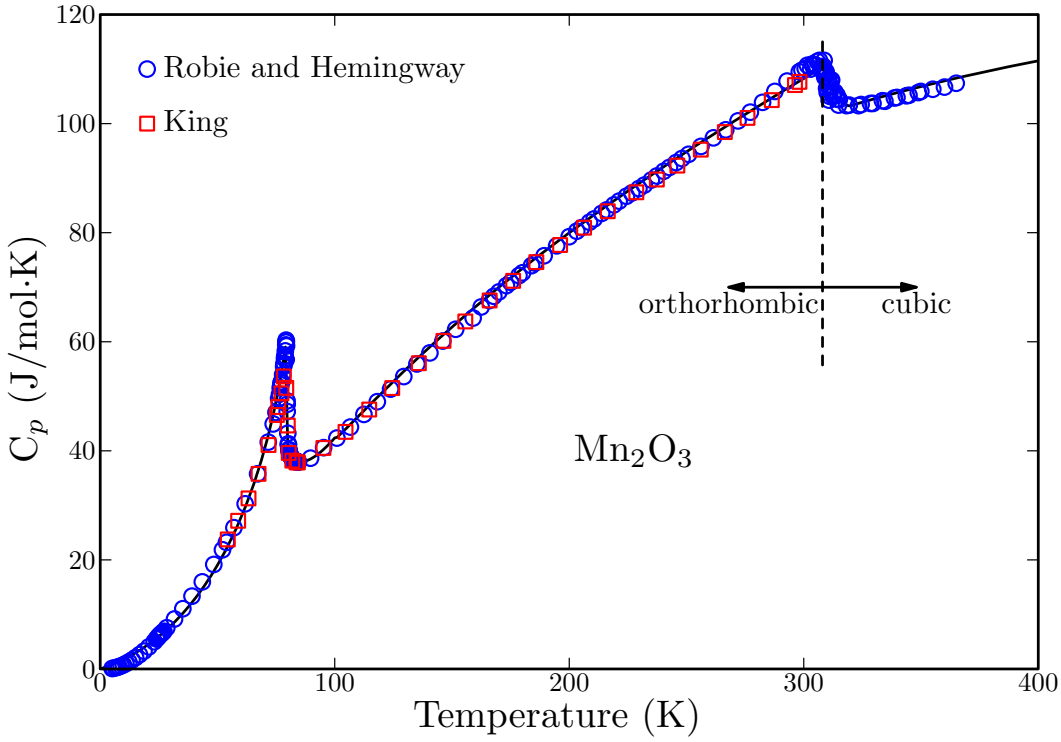

Fig. 3—Optimized heat capacity of α- and β-Mn_2O_3 along with experimental data.[27,30]

Heat contents of Mn_3O_4, Mn_2O_3, and MnO_2 were also measured calorimetrically by Fritsch and Navrotsky,[32] Southard and Moore,[33] Orr,[34] and Moore.[35] A discontinuity of heat content of Mn_3O_4 at 1441 K to 1448 K (1168 °C to 1175 °C) associated with ~20 kJ/mol was observed by Southard and Moore.[33] This corresponds to the enthalpy of transformation from tetragonal to cubic structure of the Mn_3O_4 spinel.

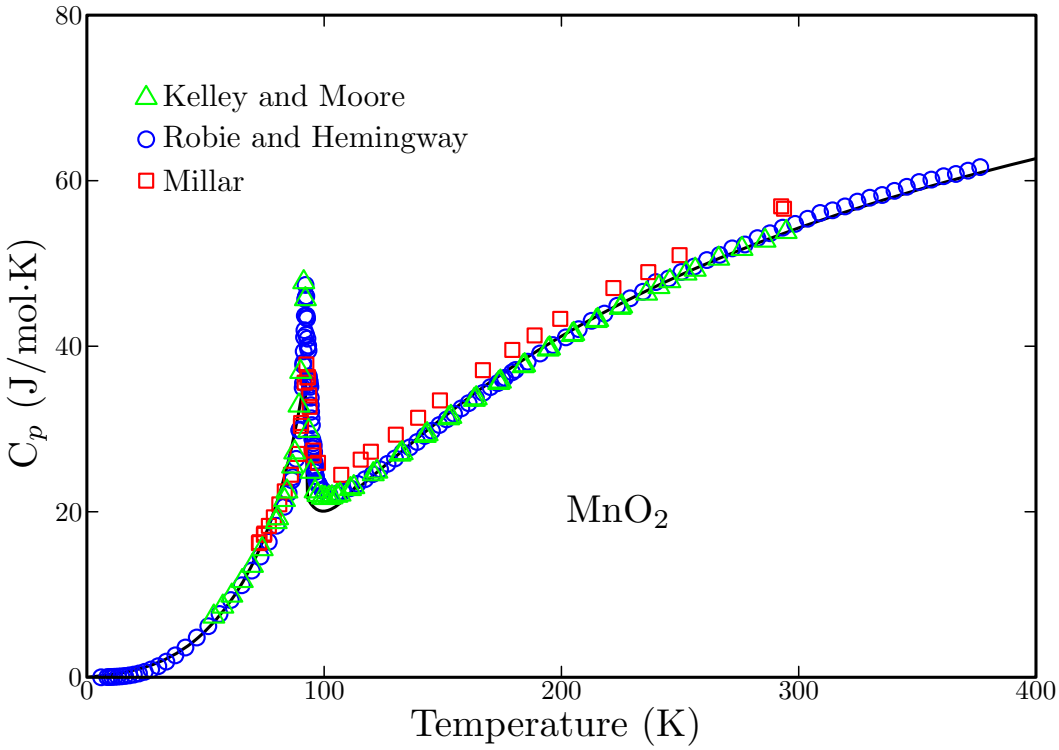

Fig. 4—Optimized heat capacity of MnO_2 along with experimental data.[26,27,29]

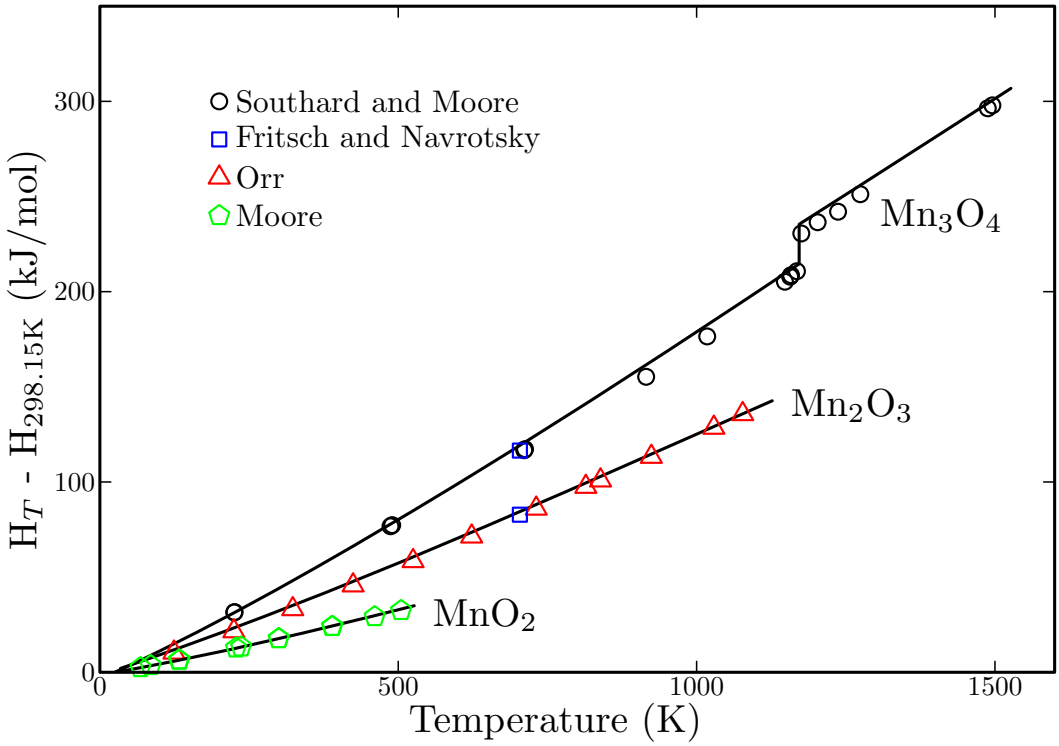

Fig. 5—Optimized heat contents of α- and β-Mn_3O_4, β-Mn_2O_3, and MnO_2 along with experimental data.[32–35]

Optimized heat contents for these phases are in good agreement with the measured data as shown in Figure 5.

B. *Valence State in Spinel*

The valence state of cations in Mn_3O_4 is still controversial. Some investigations suggested "2+/4+"

structure ($Mn_2^{2+}Mn^{4+}O_4$),[36–38] while others are in favor of the "2+/3+" structure ($Mn^{2+}Mn_2^{3+}O_4$).[39–41] In spite of this controversy, it is generally accepted that Mn_3O_4 is almost normal spinel due to high site preference energies of Mn^{3+} and Mn^{4+} for octahedral sites,[42–44] and Mn^{3+} in octahedral site is in charge of tetragonal distortion of spinel containing Mn.[40]

A later investigation by Dorris and Mason[45] using thermopower measurement on electrical properties and cation valences in Mn_3O_4 suggested that "2+/3+" structure cannot explain the electrical properties of the cubic Mn_3O_4. They observed a sudden increase of electrical conductivity and decrease of thermopower by passing the tetragonal-to-cubic transformation temperature. This implies a significant change of valence status between these two spinels. For the tetragonal Mn_3O_4, they concluded that the "2+/3+" structure is reasonable on the basis of a direct relationship between the concentration of octahedral Mn^{3+} and the tetragonal-to-cubic transformation temperature,[46,47] and the high transformation temperature in Mn_3O_4. On the other hand, in order to see feasibility the "2+/3+" structure for the cubic Mn_3O_4, they considered the following cation distribution reaction in sublattices:

$$Mn_T^{2+} + Mn_O^{3+} \Leftrightarrow Mn_O^{2+} + Mn_T^{3+} \qquad \Delta H_{dis}\,, \qquad [18]$$

where values for the ΔH_{dis} have been estimated in the range of 75 to 80 kJ/mole.[42,43] Assuming that conduction can occur on either tetrahedral or octahedral sites, not simultaneously on both sites, they considered four possible conduction models for the cubic Mn_3O_4 as follows:

1. The conduction occurs on octahedral sites by electron holes.
2. The conduction occurs on tetrahedral sites by electron holes.
3. The conduction occurs on octahedral sites by electrons.
4. The conduction occurs on tetrahedral sites by electrons.

Using the above four models along with appropriate site balance equation and the measured thermopower data, they showed that the models (1) and (3) gave site fraction of Mn^{3+} on tetrahedral site to be higher than 1. Also, derived enthalpy of the distribution reaction from the models 2 and 4 is calculated to be only 15 to 45 kJ/mole, as opposed to the reported values of 75 to 80 kJ/mole.[42,43] Moreover, non-insulating characteristic of cubic Mn_3O_4 compared to near insulation of tetragonal Mn_3O_4 implies that the "2+/3+" structure is not appropriate to the cubic Mn_3O_4, since the conduction can occur by electrons or electron holes between Mn^{2+} and Mn^{3+} in spite of high octahedral preference energy of Mn^{3+}. Hence, they employed an alternate model in which Mn^{4+} was considered in octahedral sites along with Mn^{2+} and Mn^{3+}, while tetrahedral sites are assumed to be occupied solely by Mn^{2+} due to high octahedral site preference energies of Mn^{3+} and Mn^{4+}. The following "disproportionate equilibrium" was considered:

$$2Mn_O^{3+} = Mn_O^{2+} + Mn_O^{4+} \qquad \Delta G_D\,. \qquad [19]$$

After careful considerations, they concluded that conduction proceeds by the hopping of electron holes between Mn^{4+} and Mn^{3+} on octahedral sites. Other conduction mechanisms (conduction by the hopping of electrons or electron holes between Mn^{2+} and Mn^{3+}, or conduction by the hopping of electrons between Mn^{3+} and Mn^{4+}) seemed unlikely. Therefore, in the present study, the valence status of cubic spinel was followed by the suggestion of Dorris and Mason in which Mn^{2+}, Mn^{3+}, and Mn^{4+} mix each other in octahedral site, while Mn^{2+} is the only constituent in tetrahedral site, as seen in Eq. [10]. This is also confirmed by recent electrical conductivity measurement on manganese chromite ($MnCr_2O_4$) of Lu *et al.*[48] that the Mn_2CrO_4 can be thought as $(Mn^{2+})^T[Mn^{2+}, Mn^{3+}, Mn^{4+}, Cr^{3+}]_2^OO_4$. (Manganese chromite was already modeled in the framework of the present spinel modeling by one of the present authors,[9] keeping consistency to this observation.)

For the tetragonal Mn_3O_4, the usual "2+/3+" model was used, as seen in Eq. [3]. Moreover, vacancy was also considered on octahedral sites for both Mn_3O_4 in order to model non-stoichiometries, although it is known to be very small.[3] However, it is also required to incorporate this spinel model into large spinel database already developed.[22]

Figure 6 shows the mole number of cations in each site per mole of Mn_3O_4 for tetragonal and cubic Mn_3O_4, derived from appropriate conduction mechanisms along with the measured thermopower data by Dorris and Mason,[45] as symbols. Lines in the Figure 6 are calculated in the present study. In order to reproduce the derived cation valencies in these spinels, Δ_{JL} for the cubic spinel and I_{JK} and Δ_{JK} for the tetragonal spinel were optimized. As seen in the figure, Mn^{3+} on octahedral site becomes dominant species during cubic-to-tetragonal transformation at 1445 K (1172 °C) in accord with the high preference energy of octahedral site of Mn^{3+}.

C. *Non-stoichiometry in Manganosite and Spinel*

Manganosite ($Mn_{1-x}O$) has a non-stoichiometry toward oxygen due to oxidation of Mn ($Mn^{2+} \rightarrow Mn^{3+}$) under high oxygen partial pressure. Contrary to wüstite ($Fe_{1-x}O$), the manganosite has also a non-stoichiometry toward Mn ($-0.128 < x < 0$).[49] However, in the present study, only the non-stoichiometry toward oxygen was considered. Defect mechanism of the non-stoichiometry has generally been known to be cation vacancy.[50–54] However, most of those researches showed that a single defect species does not applicable over wide range of oxygen partial pressure. For example, experimental data of non-stoichiometry by Keller and Dieckmann[53] showed that isotherms of log x (measured by TGA) *vs* log p_{O_2} do not vary linearly. This implies that more than one defect species play in the manganosite. However, for the sake of simplicity, only

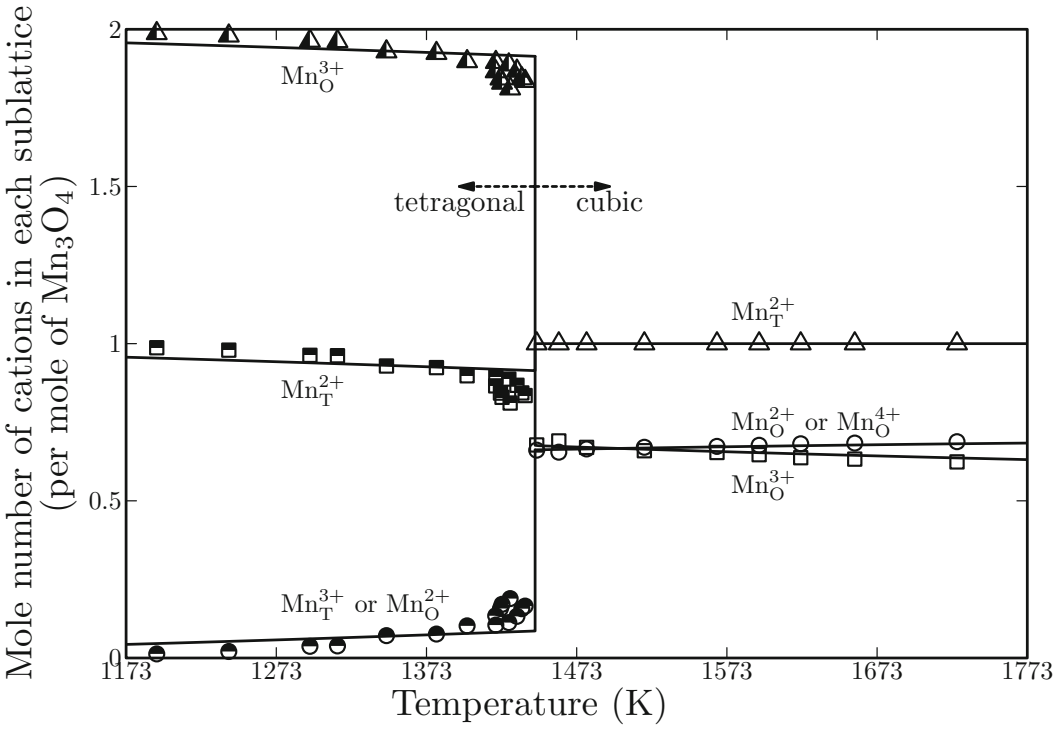

Fig. 6—Calculated cation distributions in α- and β-Mn_3O_4. For details, see Section III–B. Experimental data were taken from thermopower measurement.[45]

neutral cation vacancy associated with Mn^{3+} in cationic site was considered in the present study. Figure 7 shows the measured defect concentration as functions of oxygen partial pressure at different temperatures. Lines are calculated in the present study assuming only the neutral cation vacancy as defect species. Agreement between experiments and calculations seems reasonable.

Non-stoichiometries of both α- and β-Mn_3O_4 are very small, and those were neglected in previous thermodynamic assessments.[1,2] In fact, thermogravimetrically measured non-stoichiometry of β-Mn_3O_4 is maximum 0.05% of total cation site.[53] However, in order to keep consistency with already developed spinel model by Degterov *et al.*[22] and extend thermodynamic database for spinel solid solution, it was tried to model the non-stoichiometries of spinels in the present study. For the α-Mn_3O_4, it was assumed that the vacancy in the octahedral site was generated due to the dissolution of hypothetical "γ-Mn_2O_3." For the β-Mn_3O_4, however, it was assumed that no Mn^{3+} ion in tetrahedral site exists. Consequently, the same approach for tetragonal spinel could not be applicable. Therefore, as suggested by Degterov *et al.*,[22] the parameter V_x was fitted to the experimental data of oxygen non-stoichiometry, directly. Figures 8 and 9 show the calculated non-stoichiometries in α- and β-Mn_3O_4 along with experimental data by Keller and Dieckmann.[3] Non-stoichiometry toward MnO was neglected, and the corresponding experimental data by Keller and Dieckmann[53] are not shown. Hahn and Muan also carried out to measure excess oxygen in Mn_3O_4 using quenching and titration analysis.[55] However, their results of non-stoichiometry of $Mn_{3-x}O_4$ was quiet larger (x up to 0.008) than those of Keller and Dieckmann[3] (x up to 0.0015) and scattered. Therefore, the data of Hahn and Muan[55] was not considered in the present study.

D. *Equilibrium Oxygen Partial Pressures*

In the Mn-O system, the following redox reactions can be considered:

$$3Mn_{1-x}O + \frac{1-4x}{2}O_2 = (1-x)Mn_3O_4\,, \qquad [20]$$

$$2Mn_3O_4 + \frac{1}{2}O_2 = 3Mn_2O_3\,, \qquad [21]$$

$$Mn_2O_3 + \frac{1}{2}O_2 = 2MnO_2\,. \qquad [22]$$

A number of investigations have been carried out in order to measure the equilibrium oxygen partial pressure of the above reactions using EMF or manometer. Extensive review on these investigations are given by Grundy *et al.*[2] The measured experimental data[56–65] are compared along with the calculations in the present study and shown in Figure 10. Experimental data (equilibrium oxygen partial pressure) for the Reaction [20] are in generally good agreement with those

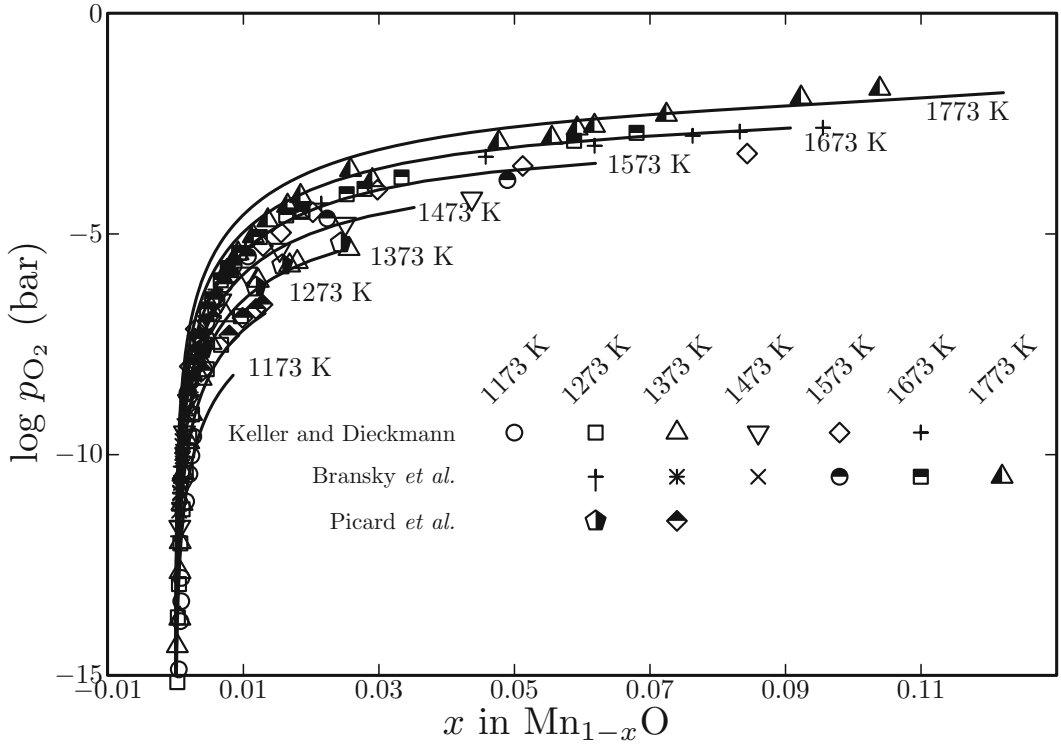

Fig. 7—Calculated oxygen partial pressures over manganosite at various temperatures along with experimental data.[51–53]

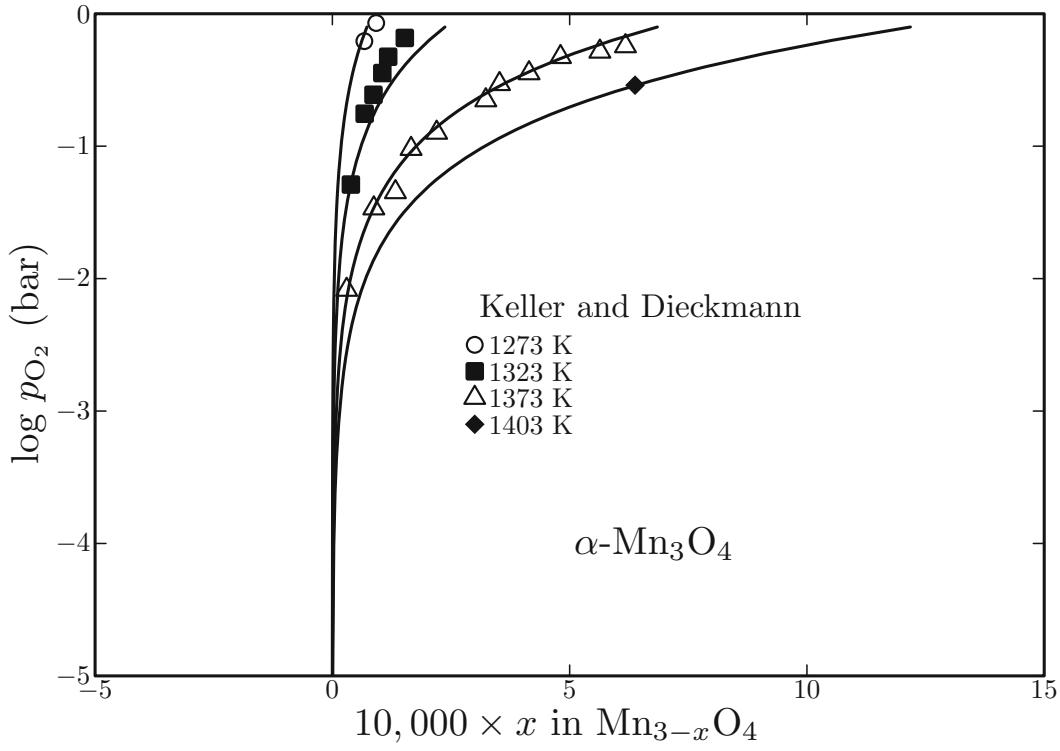

Fig. 8—Calculated oxygen partial pressures over α-Mn_3O_4 at various temperatures along with experimental data.[3]

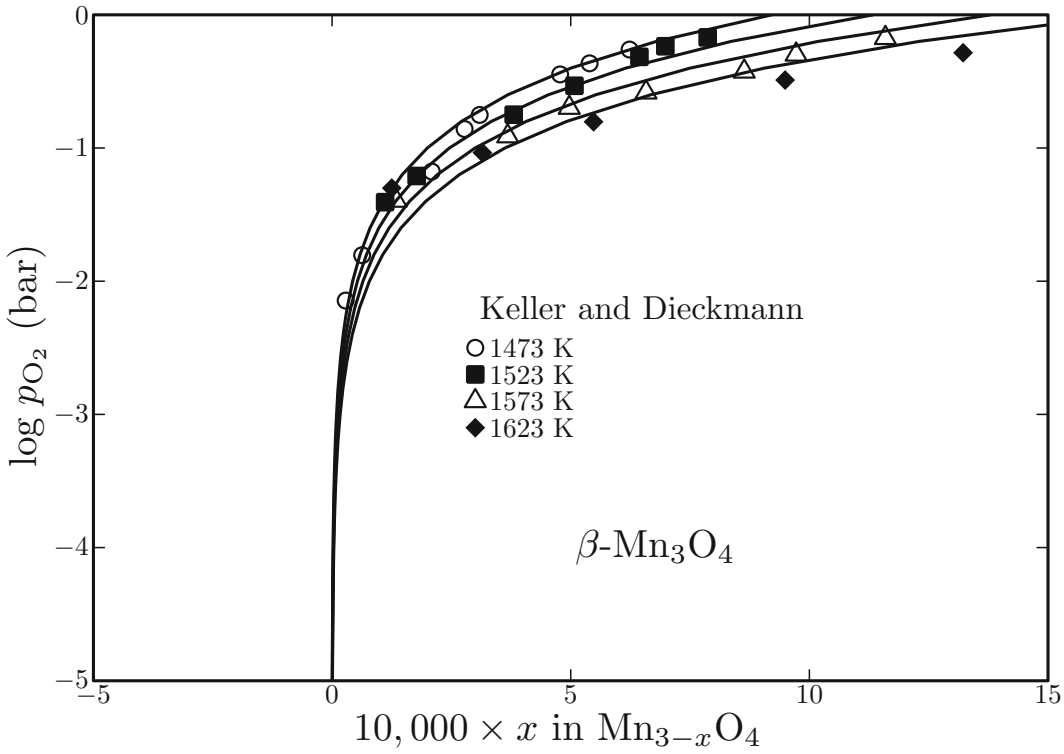

Fig. 9—Calculated oxygen partial pressures over β-Mn_3O_4 at various temperatures along with experimental data.[3]

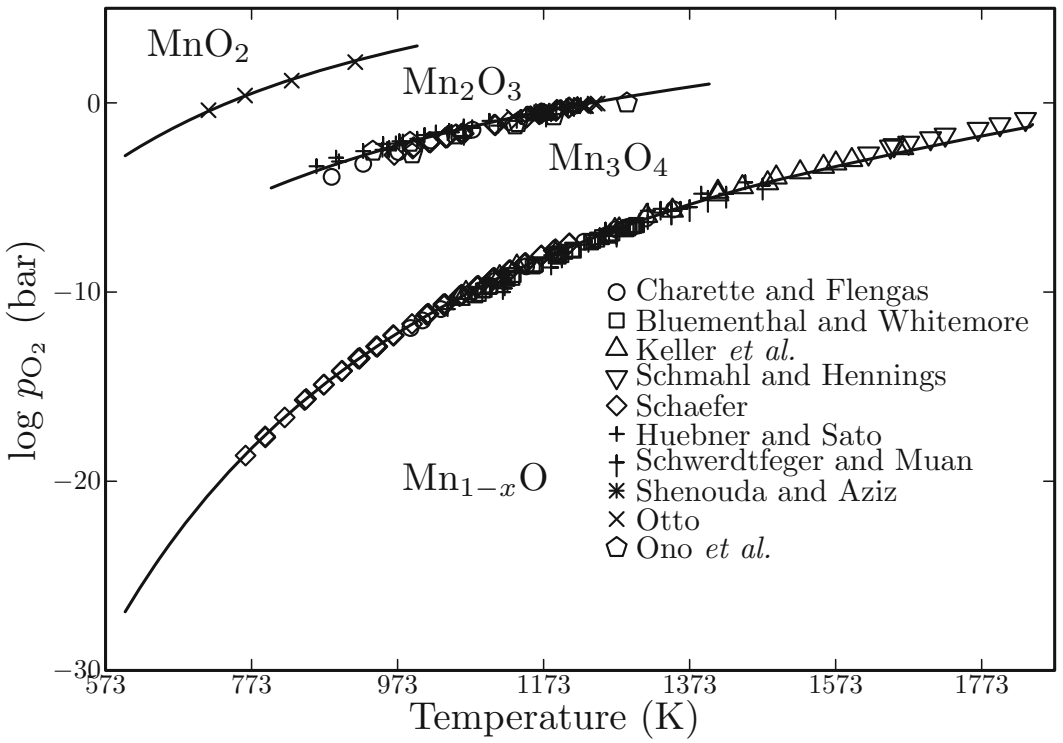

Fig. 10—Calculated oxygen partial pressures in three-phase equilibria (gas phase with $Mn_{1-x}O$-Mn_3O_4, Mn_3O_4-Mn_2O_3, Mn_2O_3-MnO_2), as functions of temperature, along with experimental data.[56–59,61–65]

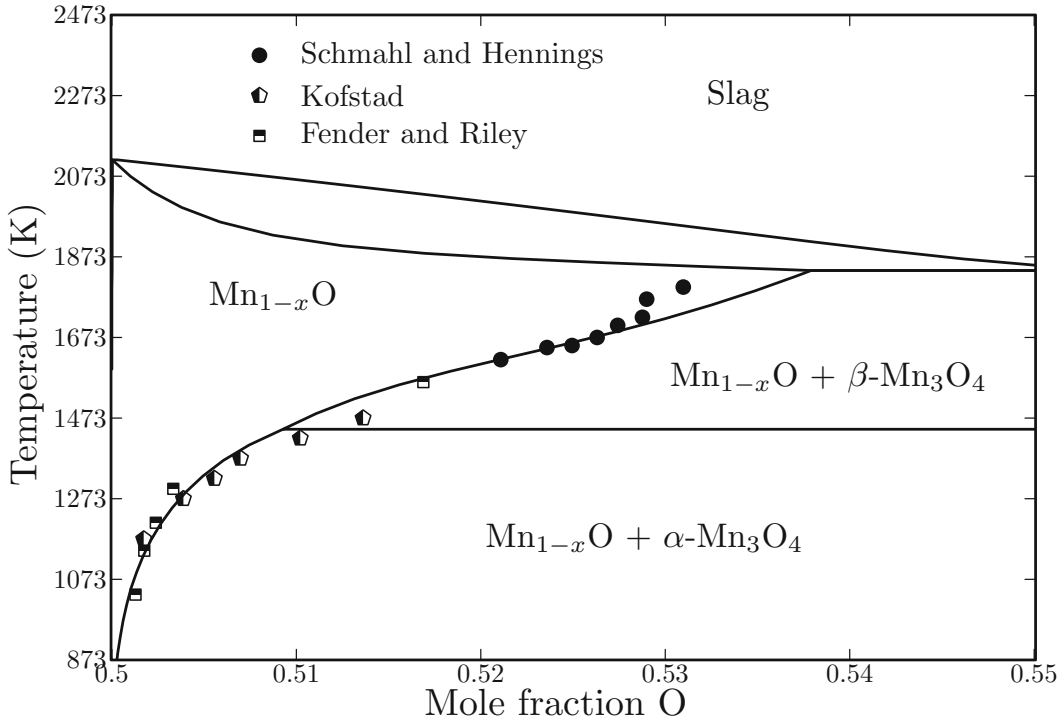

Fig. 11—Enlarged phase diagram at $Mn_{1-x}O$ region along with experimental data.[54,64,71]

investigations. Scatter of the reported data for the Reaction [21] at low temperature is probably due to hysteresis between redox Reaction [21].[66] In the present study, experimental data which were obtained relatively high temperature by Shenouda and Aziz[66] and Otto[58] were preferred for the Reaction [21]. For the Reaction [22], experimental data of Otto[59] was used due to relatively longer experimental time.

E. *Phase Diagrams*

Figure 1 shows the optimized phase diagram of the Mn-O system with the oxygen partial pressure and temperature as axis variables. Several phase-equilibrium data measured mainly using quenching and XRD are shown as symbols.[20,21,55,67–70] It should be noted that the dashed lines are only predicted by the model because there is no experimental data available. Also, in the present study, the molten oxide phase is defined up to $X_O = 0.6$ which corresponds to the hypothetical pure liquid "Mn_2O_3". Therefore, the liquidus of MnO_2 is only imaginary and is pending to further experimental verification. Calculated phase boundary of manganosite in equilibrium with α- and β-Mn_3O_4 are shown in Figure 11 along with measured experimental data.[54,64,71] The concentration range of the manganosite becomes wide quickly as temperature increases, due to dissolution of Mn^{3+}. In order to reproduce this and the equilibrium oxygen partial pressures over the manganosite, one interaction parameter and Gibbs energy of dissolution of $MnO_{1.5}$ in the manganosite solution were optimized (Table III). Also in order to reproduce liquidus of manganosite and β-Mn_3O_4,[20,21,69] Gibbs energy of the hypothetical pure liquid "$MnO_{1.5}$" was used as a model parameter (Table III). Since there is no further experimental data for the slag in the Mn-O system, it was decided not to use interaction parameter between Mn^{2+} and Mn^{3+}. At the present stage, it has been found that the current description of the Mn-O molten oxide phase results in a good agreement with reported experimental data in multicomponent systems containing up to Fe, Cr, Mn, Si, and O from metal saturation to 1 atm O_2 atmosphere. The details of the thermodynamic optimization for these systems will be shown elsewhere.[9–11]

From the present thermodynamic optimization, the phase diagram of Mn-O system with oxygen iso-bar was drawn as shown in Figure 12(a) from MnO to MnO_2. Gas phase was suspended during the calculation. Again, part of the calculated phase diagram at high oxygen partial pressure ($\log p_{O_2} > \sim 0$) is imaginary and only predicted by thermodynamic models. Nevertheless, since the non-stoichiometries of α- and β-Mn_3O_4 were considered by introducing the vacancies, it could be observed that the spinel solutions deviate from its stoichiometric composition as the oxygen partial pressure increases. A similar phase diagram reported by Grundy *et al.* is also shown in Figure 12(b) for a comparison.

Various special points including invariant reactions are calculated using the models of the present study and are shown in Table IV. Other calculated values from previous thermodynamic modeling[1,2] are also compared.

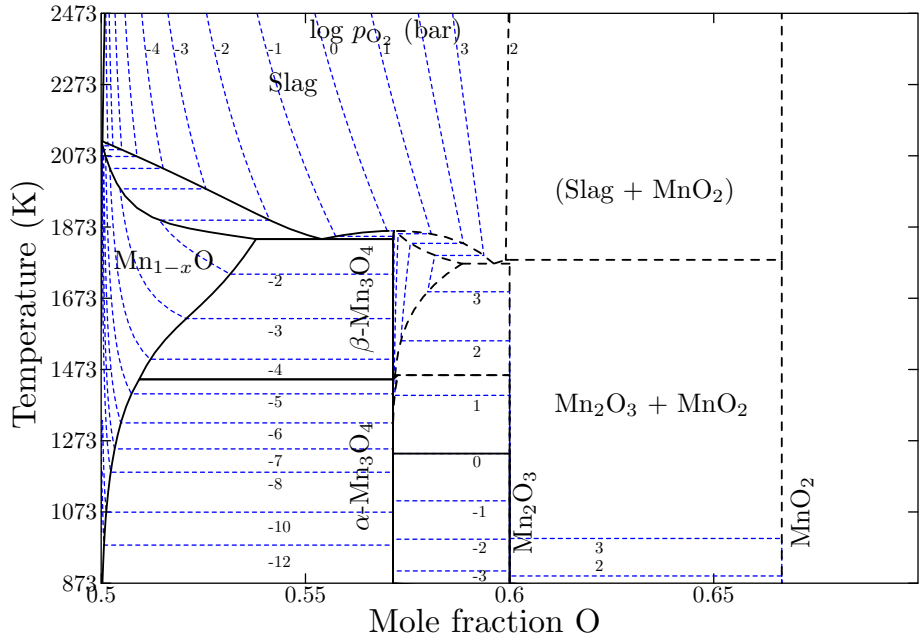

(a)

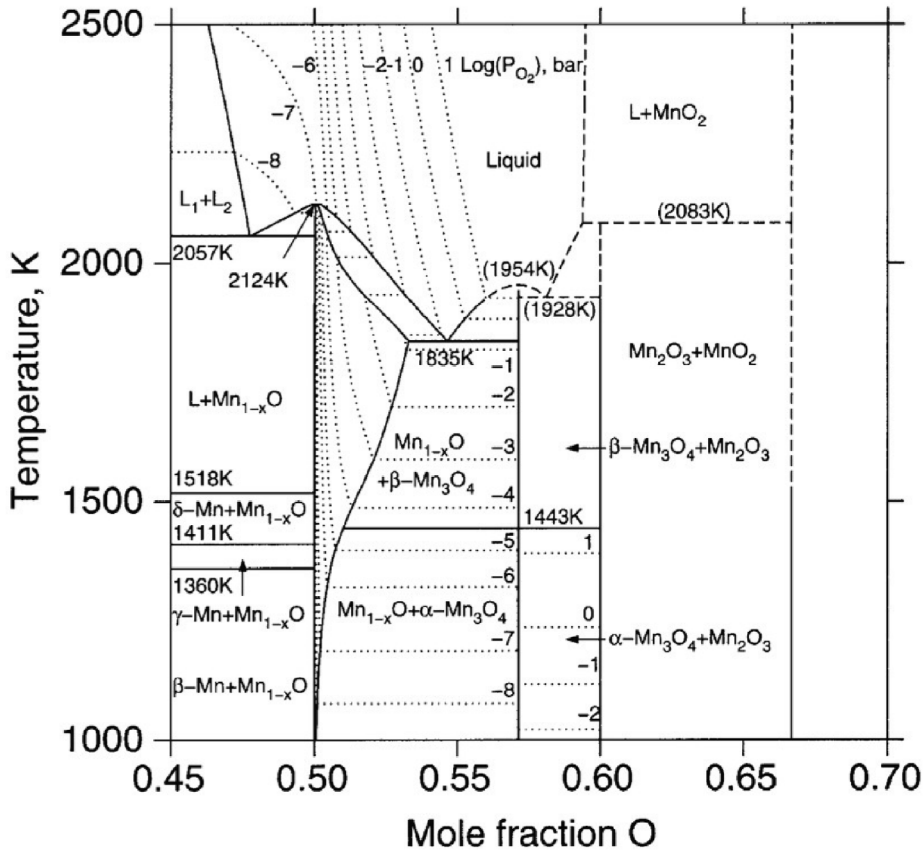

(b)

Fig. 12—Calculated phase diagram of the Mn-O system in the range of composition (*a*) from $X_O = 0.5$ to $X_O = 0.7$ in the present study (modified from a figure presented in Ref. [12]), and (*b*) from $X_O = 0.45$ to $X_O = 0.7$, reprinted with permission from Grundy *et al.*[2] Dashed lines are oxygen iso-bars.

Table IV. Special Points Including Invariant Reactions Involving Oxides in Mn-O System

Reaction	Temperature in Kelvin (T in [K (°C)])		Reference
Slag → $Mn_{1-x}O$ + βMn_3O_4		1839 (1566)	Present study
	1833 (1560)		Wang and Sundman[1]
	1835 (1562)		Grundy *et al.*[2]
Slag → βMn_3O_4		1862 (1589)	Present study
	—		Wang and Sundman[1]
	1954 (1681)		Grundy *et al.*[2]
Slag → βMn_3O_4 + β-Mn_2O_3		1770 (1497)	Present study
	—		Wang and Sundman[1]
	1928 (1655)		Grundy *et al.*[2]
βMn_3O_4 → $Mn_{1-x}O$ + αMn_3O_4		1445 (1172)	Present study
	1448 (1175)		Wang and Sundman[1]
	1443 (1170)		Grundy *et al.*[2]
βMn_3O_4 + β-Mn_2O_3 → αMn_3O_4		1457 (1184)	Present study
	1448 (1175)		Wang and Sundman[1]
	1443 (1170)		Grundy *et al.*[2]

IV. CONCLUSION

A critical evaluation/optimization of experimental data for the Mn-O system was performed in the present study. The optimized model parameters can reproduce all reliable thermodynamic and structural data as well as the phase diagrams of the Mn-O system within experimental error limits. In order to construct a larger thermodynamic database, α- and β-Mn_3O_4 were modeled as a part of spinel solid solutions. This enables us to integrate the presently developed database into a larger thermodynamic database. The database of model parameters can be used with general thermodynamic software, such as FactSage,[13,14] in order to calculate the thermodynamic properties, the distribution of cations in the spinel solutions which is related to the electrical properties of the spinel, and phase equilibria for temperatures, compositions, and oxygen partial pressures where experimental data are not available. The present thermodynamic modeling has been extended to incorporate Cr,[9] Fe,[10] and Si,[11] respectively.

REFERENCES

1. M. Wang and B. Sundman: *Metall. Trans. B.*, 1992, vol. 23B, pp. 821–31.
2. A.N. Grundy and L. Gauckler: *J. Phase Equilib.*, 2003, vol. 24, pp. 21–39.
3. M. Keller and R. Diekmann: *Ber. Bunsenges Phys. Chem.*, 1985, vol. 89, pp. 1095–1104.
4. M. Hillert, B. Jansson, and B. Sundman: *Z. Metallkd.*, 1988, vol. 79, pp. 81–87.
5. M. Hillert, B. Jansson, B. Sundman, and J. Ågren: *Metall. Trans. A.*, 1985, vol. 16A, pp. 261–66.
6. M. Kowalski, P. Spencer, and D. Neuschütz: *Slag Atlas*, 2nd ed., Verlag Stahleisen GmbH, Düsseldorf, Germany, 1995, Chap.3, Phase diagrams.
7. S. Decterov, I.-H. Jung, Y.-B. Kang, E. Jak, V. Swamy, D. Kevorkov, A.D. Pelton: Tech. Report, École Polytechnique de Montréal, Montréal, QC, Canada, 2002.
8. L. Kjellqvist and M. Selleby: *J. Phase Equilib. Diffus.*, 2010, vol. 31, pp. 113–34.
9. I-H Jung: *Solid State Ion.*, 2006, vol. 177, pp. 765–77.
10. Y.-B. Kang and I.-H. Jung: Korea, Unpublished Research, POSTECH, 2016.
11. Y.-B. Kang, I.-H. Jung: Korea, Unpublished Research, POSTECH, 2016.
12. Y.-B. Kang and I.-H. Jung: *Proc. of 8th Int. Conf. on Molten Slags, Fluxes, and Salts*, Gecamin Ltd., Santiago, Chille, 2009, pp. 459–71.
13. C.W. Bale, P. Chartrand, S. Degterov, G. Eriksson, K. Hack, R.B. Mahfoud, J. Melançon, A.D. Pelton, and S. Petersen: *CALPHAD*, 2002, vol. 26, pp. 189–28.
14. C.W. Bale, E. Bélisle, P. Chartrand, S. Decterov, G. Eriksson, K. Hack, I.-H. Jung, Y.-B. Kang, J. Melançon, A.D. Pelton, C. Robelin, and S. Petersen: *CALPHAD*, 2009, vol. 33, pp. 295–311.
15. A.D.Pelton and M. Blander: *Proc. of the 2nd Int. Symp. on Metallurgical Slags and Fluxes*, TMS-AIME, Warrendale, PA, 1984, pp. 281–94.
16. A.D. Pelton and M. Blander: *Metall. Trans. B.*, 1986, vol. 17B, pp. 805–15.
17. A.D. Pelton, S. Degterov, G. Eriksson, C. Robelin, and Y. Dessureault: *Metall. Mater. Trans. B.*, 2000, vol. 31B, pp. 651–59.
18. A.D. Pelton and P. Chartrand: *Metall. Mater. Trans. A.*, 2001, vol. 32A, pp. 1355–60.
19. P. Wu, G. Eriksson, and A.D. Pelton: *J. Am. Ceram. Soc.*, 1993, vol. 76, pp. 2065–75.
20. A. Hed and D. Tannhauser: *J. Electrochem. Soc.*, 1967, vol. 114, pp. 314–18.
21. G. Trömel, W. Fix, K. Koch, and F. Schaberg: *Erzmetall.*, 1976, vol. 29, pp. 234–37.
22. S. Degterov, E. Jak, P. Hayes, and A.D. Pelton: *Metall. Mater. Trans. B.*, 2001, vol. 32B, pp. 643–57.
23. A. Dinsdale: *CALPHAD*, 1991, vol. 15, pp. 317–425.
24. G. Inden: GmbH, Düsseldorf, Germany, Max-Planck-Inst. Eisenforschung, 1976, p. 111.
25. M. Hillert and M. Jarl: *CALPHAD*, 1978, vol. 2, pp. 227–38.
26. R. Millar: *J. Am. Chem. Soc.*, 1927, vol. 50, pp. 1875–83.
27. R. Robie and B. Hemingway: *J. Chem. Thermodyn.*, 1985, vol. 17, pp. 165–81.
28. K. Chhor, J. Bocquet, and C. Pommier: *J. Chem. Thermodyn.*, 1986, vol. 18, pp. 89–99.
29. K. Kelley and G. Moore: *J. Am. Chem. Soc.*, 1943, vol. 65, pp. 782–85.
30. E. King: *J. Am. Chem. Soc.*, 1954, vol. 76, pp. 3289–91.
31. S. Geller and G. Espinosa: *Phys. Rev. B.*, 1954, vol. 1, pp. 3763–69.
32. S. Fritsch and A. Navrotsky: *J. Am. Ceram. Soc.*, 1996, vol. 79, pp. 1761–68.
33. J. Southard and G. Moore: *J. Am. Chem. Soc.*, 1942, vol. 64, pp. 1769–70.
34. R. Orr: *J. Am. Chem. Soc.*, 1954, vol. 76, pp. 857–58.
35. G. Moore: *J. Am. Ceram. Soc.*, 1943, vol. 65, pp. 1398–99.
36. W. Fyfe: *Nature (Lond.)*, 1949, vol. 164, p. 790.
37. F. Romeijin: *Philips Res. Rep.*, 1953, vol. 8, pp. 304–42.
38. M. Fine and C. Chiou: *Phys. Rev.*, 1957, vol. 1, pp. 121–22.

39. R. Metselaar, R.V. Tol, and P. Piercy: *J. Solid State Chem.*, 1981, vol. 38, pp. 335–41.
40. J. Dunitz and L. Orgel: *J. Phys. Chem. Solids*, 1957, vol. 3, pp. 20–29.
41. M. O'Keefe: *J. Phys. Chem. Solids*, 1961, vol. 21, pp. 172–78.
42. A. Navrotsky and O. Kleppa: *J. Inorg. Nucl. Chem.*, 1967, vol. 29, pp. 2701–14.
43. A.D. Pelton, H. Schmalzried, and J. Sticher: *Ber. Bunsenges Phys. Chem.*, 1979, vol. 83, pp. 241–52.
44. H. O'Neill and A. Navrotsky: *Am. Mineral.*, 1984, vol. 69, pp. 733–53.
45. S. Dorris and T. Mason: *J. Am. Ceram. Soc.*, 1988, vol. 71, pp. 379–85.
46. V. Brabers: *J. Phys. Chem. Solids*, 1971, vol. 32, pp. 2181–91.
47. M. Rosenberg, P. Nicolau, R. Manaila, and P. Pausescu: *J. Phys. Chem. Solids*, 1963, vol. 24, pp. 1419–34.
48. Z. Lu, J. Zhu, E. Payzant, and M. Paranthaman: *J. Am. Ceram. Soc.*, 2005, vol. 88, pp. 1050–1053.
49. Q. Chen: *Acta Metall. Sin.*, 1988, vol. 24, pp. B440–42.
50. A. Hed and D. Tannhauser: *J. Chem. Phys.*, 1967, vol. 47, pp. 2090–103.
51. C. Picard and P. Gerdanian: *J. Solid State Chem.*, 1974, vol. 11, pp. 190–202.
52. I. Bransky and N. Tallan: *J. Electrochem. Soc.*, 1971, vol. 11, pp. 788–93.
53. M. Keller and R. Diekmann: *Ber. Bunsenges Phys. Chem.*, 1985, vol. 89, pp. 883–93.
54. P. Kofstad: *J. Phys. Chem. Solids*, 1983, vol. 44, pp. 879–89.
55. W. Hahn and A. Muan: *Am. J. Sci.*, 1960, vol. 258, pp. 66–78.
56. J. Huebner and M. Sato: *Am. Mineral.*, 1970, vol. 55, pp. 934–52.
57. K. Schwerdtfeger and A. Muan: *Trans. Metall. Soc. AIME*, 1967, vol. 239, pp. 1114–19.
58. E. Otto: *J. Electorchem. Soc.*, 1964, vol. 111, pp. 88–92.
59. E. Otto: *J. Electorchem. Soc.*, 1965, vol. 112, pp. 367–70.
60. K. Ono, T. Ueda, T. Ozaki, Y. Ueda, A. Yamaguchi, and J. Moriyama: *Nippon Kinzoku Gakkaishi*, 1971, vol. 35, pp. 757–63.
61. G. Charette and S. Flengas: *J. Electrochem. Soc.*, 1968, vol. 115, pp. 796–804.
62. R. Blumenthal and D. Whitemore: *J. Am. Ceram. Soc.*, 1961, vol. 44, pp. 508–12.
63. M. Keller, J. Xue, and R. Diekmann: *J. Electrochem. Soc.*, 1991, vol. 138, pp. 3393–3401.
64. N. Schmahl and D. Hennings: *Arch. Eisenhüttenwes*, 1969, vol. 40, pp. 395–99.
65. S. Schaefer: Tech. Report, Bureau of Mines, United States Department of the Interior, Washington DC, 1982.
66. F. Shenouda and S. Aziz: *J. Appl. Chem.*, 1967, vol. 17, pp. 258–62.
67. H.V. Hook and M. Keith: *Am. Mineral.*, 1958, vol. 43, pp. 69–83.
68. M. Davies and F. Richardson: *Trans. Farad. Soc.*, 1959, vol. 55, pp. 604–10.
69. H.V. Warthenberg, H. Reusch, E. Saran, and Z. Anorg: *Allg. Chem.*, 1937, vol. 230, pp. 257–76.
70. A. Muan and S. Somiya: *Am. J. Sci.*, 1962, vol. 260, pp. 230–40.
71. B. Fender and F. Riley: *Chem. Extended Defects Non-Metal Solids*, North Holland, Amsterdam, The Netherlands, 1970, pp. 54–61.